RSC Applied Interfaces

ROYAL SOCIETY OF CHEMISTRY

PAPER

View Article Online
View Journal | View Issue

Cite this: *RSC Appl. Interfaces*, 2025, **2**, 1407

Supercritical preparation of doped (111) facetted nickel oxide for the oxygen evolution reaction†

Elliot Brim, [a] Darius Hayes,[a] Konstantin Kimone Rücker, [cd] Dereje Hailu Taffa, [d] Omeshwari Bisen, [e] Marcel Risch, [e] Shaun Alia,[b] Julian Lorenz, [c] Corinna Harms, [c] Michael Wark [d] and Ryan M. Richards *[ab]

Received 19th June 2025,
Accepted 11th July 2025

DOI: 10.1039/d5lf00174a

rsc.li/RSCApplInter

Green hydrogen is of great interest as a replacement for traditional fossil fuels in a variety of energy applications. However, due to the poor kinetics present in the oxygen evolution reaction (OER) half-reaction, nanostructured catalysts are needed to reduce the reaction overpotential. Nickel oxide has previously been shown to be a promising alternative to expensive Pt-group based catalysts for the OER in alkaline media. Herein, facetted NiO nanosheets have been doped with Fe, Mn, or Co to reduce its catalytic overpotential for the OER. A supercritical synthesis process was used to promote the mass transport of the reactants while preserving catalytic surface area. Microscopy, diffraction, spectroscopy, and adsorption techniques were used to understand the morphological changes resulting from the inclusion of each dopant, as well as characterize the surface chemistry presented by the doped (111) facet. The pH was found to affect the properties of mixing due to difference in hydrolysis rates and catalysis of the hydrolysis/condensation. The dopants exhibited distinct effects on OER activity: Mn increased the overpotential to 742 mV *vs.* RHE, while Co and Fe reduced it to 502 mV and 457 mV, respectively. In summary, a straightforward and novel synthesis method is presented to prepare doped NiO(111) nanosheets, and their surface characteristics are explored to understand their varied electrochemical performances.

Introduction

Nanostructuring of 1-D or 2-D metal oxides has shown promise in several technological areas including catalysis, energy storage, and carbon capture and therefore have been a large focus in recent research involving catalyst development, batteries, and carbon sequestration.[1,2] Nano-designed catalysts provide the benefits of high surface area, tuneable surface chemistry, and other interface-related properties that lead to increased activity. In the energy field there has been a push to find economically viable ways to produce green hydrogen, or hydrogen made through electrolysis, as a replacement to liquid fossil fuels.[3] In the electrolysis process there are two half reactions occurring: the oxygen evolution reaction (OER) and the hydrogen evolution reaction (HER). Of the two reactions, the OER is energetically a bottleneck as the 4-electron transfer process results in sluggish kinetics.[4] Therefore catalysts are required to lower this energetic barrier to industrial viable levels.

Platinum group metals (PGMs) currently are the most effective catalysts for the OER.[5,6] However, their high cost and limited global availability pose significant challenges for large-scale deployment.[7] PGMs are typically used in proton exchange membrane (PEM) cells which inherit this high cost detriment.[8] As an alternative, alkaline exchange membrane (AEM) systems are electrolyzers that utilize a different pH environment allowing for a broader range of earth-abundant and cost-effective materials to be viable.[9] Among the most promising catalysts in alkaline media are metals oxides, particularly rock salt oxides, spinel oxides, and layered double hydroxides. Of these materials, NiO and $Ni(OH)_2$ have previously been shown to be a particularly active catalyst for the OER.[10,11] Under electrochemical cycling, there is a reconstruction of the catalyst surface, wherein exposed oxides or hydroxides convert into oxyhydroxides which are the electrochemically active species under operating

[a] *Department of Chemistry, Colorado School of Mines, 1500 Illinois St, Golden, Colorado 80401, USA. E-mail: rrichard@mines.edu*
[b] *Energy Systems Integration Facility, National Renewable Energy Laboratory, 15013 Denver W Pkwy, Golden, Colorado 80401, USA*
[c] *Institute of Engineering Thermodynamics, German Aerospace Center (DLR), Carl-von-Ossietzky-Str. 15, 26129 Oldenburg, Germany*
[d] *Institute of Chemistry, Chemical Technology I, Carl von Ossietzky University of Oldenburg, Carl-von-Ossietzky-Str. 9-11, 26129 Oldenburg, Germany*
[e] *Nachwuchsgruppe Gestaltung des Sauerstoffentwicklungsmechanismus, Helmholtz-Zentrum Berlin für Materialien und Energie GmbH, Hahn-Meitner-Platz 1, 14109 Berlin, Germany*

† Electronic supplementary information (ESI) available. See DOI: **https://doi.org/10.1039/d5lf00174a**

conditions[12–14] A key factor for catalyst performance is maximizing the available electrochemical active surface. Therefore it is valuable to study nickel oxide at the nanoscale with specific morphologies and dimensions to further improve the catalytic performance.[15]

The surface chemistry of a catalyst is strongly influenced by the specific crystallographic facet exposed at the surface.[16,17] Each facet has different electronic and geometric environments (such as interatomic distances) which result in differing adsorption energies and reaction kinetics during water oxidation.[17,18] Previously, computational studies have shown that the calculated OER activities of NiO rank as (110) > (111) > (100).[19] Of these, the (111) surface most readily forms in wet synthetic environments. NiO is a rock salt with the $Fm\bar{3}m$ space group, and when terminated along the (111) plane is dominated by oxygen on the surface.[10,16] Under OER operating conditions, this oxygen-rich surface undergoes reconstruction to form an active oxyhydroxide phase, resulting in a high density of catalytically active sites. Pristine (111) facetted NiO nanosheets have previously been synthesized and tested for the OER and showed activity comparable to if not better than NiO nanoparticles.[11] Interestingly, the overall surface area of the material is less impactful than the effective surface area provided by high crystallinity and active site density through specific faceting.

Previous literature has extensively shown that the incorporation of dopants into NiO has been found to improve the intrinsic activity of the catalysts for the OER.[20] For instance, Xiao *et al.* incorporated La to alter the d-band states of the catalyst to increase OER activity.[21] Dopants have also been employed to improve the long-term stability of nickel-based catalysts. In earlier work, Strasser *et al.* reported that Fe stabilizes the Ni^{2+} to Ni^{3+} redox transition during the *in situ* formation of oxyhydroxide species due to the higher Fe oxidation state stabilizing the Ni intermediate from overoxidizing to Ni^{4+}.[22] Etxebarria *et al.* showed that the incorporation of Fe decreased the oxyhydroxide layer thickness under operating conditions while simultaneously increasing OER activity.[23] It must be noted, however, that Fe will dope or alloy with the NiO when the KOH electrolyte is not rigorously purified within a working setup resulting in undesired phases.[24]

Co systems have also been extensively explored as potential OER catalysts with promising results being shown. Paul *et al.* demonstrated that CoO nanoparticles with tuneable morphologies result in different surface chemistries with high surface area low index facetted CoO promoting formation of CoOOH and interparticle porosity.[25] Xu *et al.* observed that while pure cobalt oxides can suffer from limited conductivity under OER conditions due to higher electrical resistance, mixing with Ni results in better conductivity through the bulk. Wang *et al.* similarly demonstrated that Co–Ni mixed systems promote the oxyhydroxide intermediate formation when in operating conditions while also providing increased stability.[6,26] Mn has been shown to form a stable hydroxyl radical on the surface of Ni catalysts and thereby increasing the density of accessible active sites for the OER.[27] Collectively, these studies highlight the importance of both surface engineering and targeted incorporation of secondary metals as effective strategies for optimizing the activity and durability of Ni-based OER catalysts.

The supercritical preparation and drying offers several advantages to a traditional wet chemical synthesis while keeping the core benefits. This method has long been employed to mitigate aggregation kinetics during solvent removal resulting in a better preservation of the as-prepared material's surface area and microstructure. In this process, reactants are first combined in solution and subsequently transferred to an autoclave. The system is then subjected to high temperature and pressure conditions which are enough to surpass the critical point of the solvent (for methanol, 262 °C and 80 bar).[28] Once above the critical stage, the solvent has liquid-like densities but gas-like viscosities which enhances the mass transfer characteristics of the solvent.[29]

As stated, the (111) facet of NiO is characterized by a high density of surface oxygen atoms, offering an ideal platform to promote the oxygen evolution reaction (OER). Employing nanosheet morphology not only promotes the preferential exposure of this catalytically active facet but also significantly enhances the electrochemically active surface area due to its architecture. In addition, the two-dimensional nature of nanosheets is expected to limit dopant diffusion into the bulk, given their reduced bulk-to-surface ratio compared to other morphologies of similar size. And the supercritical process will aid in the distribution of the reactants for a well-dispersed catalyst. While Fe–Ni systems have been extensively investigated, Co–NiO and Mn–NiO systems remain less explored, particularly in the context of AEM electrolyzers. Additionally, the systematic investigation of morphological evolution in response to varying dopant concentrations within facetted nanosheet structures is novel. Importantly, unsupported doped and facetted NiO nanosheets tailored for the OER in AEM systems are under-reported in literature. By addressing these gaps, this study aims to expand the understanding of nanoscale catalyst design and bring greater attention to their potential in advancing next-generation water-splitting technologies. Structural and surface characterization techniques such as transmission electron microscopy (TEM), X-ray diffraction (XRD), and N_2 physisorption were utilized to probe the success of secondary metal incorporation while maintaining the morphology of the material. Cyclic voltammetry (CV) is used to probe the electrochemical performance improvement of the catalyst over the pristine material.

Methods

Metal nitrate hydrates were obtained through Sigma Aldrich. The synthesis for NiO nanosheets with hexagonal holes has been previously reported.[16] Briefly, the general synthesis starts by dissolving 4.5 g of $Ni(NO_3)_2$ in 100 mL of absolute

methanol. The inclusion of additional metal nitrates occurred during this dissolution of the Ni salt, mixing the cations in solution. When introducing a second metal salt, the absolute methanol was first treated with 75% ammonium hydroxide (~0.75 mL) to create a basic solution. When the metal nitrates were dissolved into the solution, the pH stabilized to approximately 4. After fully dissolving, 0.5 g of urea is added and fully dissolved in the solution. This is followed by 3.3 g of benzyl alcohol added dropwise to the solution with stirring. The solution is then stirred for 1 h, after which it is inserted into an autoclave. The autoclave is purged with Ar several times before being charged with 8 bars of argon. The autoclave is heated to 200 °C for 4 h then raised to 265 °C for an additional 1.5 h, taking it above the critical point of methanol. After this period, the autoclave is vented and allowed to cool overnight. Once completed, a fine green powder is collected and calcined at 400 °C for 4 hours with a ramp rate of 2.5 °C min^{-1}.

Instrumentation

A Bruker D2 Phaser Benchtop powder X-ray diffraction (PXRD) with a Cu radiation source at 300 W was used to take the PXRD patterns in a range of 20–80 degrees. The Scherrer equation was used to calculate crystallite sizes. Microscopy images were taken using a FEI Talos F200X transmission electron microscope (TEM) equipped with energy dispersive X-ray spectroscopy (EDS). Samples were prepared by sonication in ethanol before drop casting on a copper grid with a carbon support mesh. High resolution imaging was done at 200 kV and lattice spacing analysis was done by measuring the distance between lattice fringes using the high-resolution magnitude range (>300 kV). ImageJ was used to calibrate according to the instrument given scale bar and measure the distance across at minimum 10 fringes. This measurement was done through multiple regions of the sample image and several different samples to confirm the exposed facet. Scanning transmission electron microscopy (STEM) mode was used to provide STEM-EDS to generate an elemental distribution map of samples. Brunauer–Emmett–Teller (BET) surface area measurements were taken with the Micromeritics ASAP 2020 Physisorption using N_2 desorption. The samples were degassed at 200 °C for 4 hours under nitrogen before the experiment was performed as previously reported.[30] Inductively coupled plasma optical emission spectroscopy (ICP-OES) was performed by using a 75% HNO_3/25% HCl digestion in a CEM MARS 6 microwave digestion system before being serial diluted to 2.4% acid concentration. X-ray absorption spectroscopy (XAS) experiments were performed at the Ni K-edge using the KMC-2 beamline at the BESSY II electron storage ring (300 mA, top-up mode) operated by Helmholtz-Zentrum Berlin für Materialien and Energie in Berlin, Germany. Detailed information about the experimental setup is provided elsewhere.[31,32] OER experiments were performed at the German Aerospace Center (DLR) located in Oldenburg, Germany. The electrochemical tests in a three-electrode setup were performed using a PTFE cell filled with 100 mL of 0.1 M KOH electrolyte (pH ~12.5) and commercial GC discs from HTW (SIGRADUR® G, 5(±0.05) mm, polished and lapped) were used as substrates. A graphite rod was used as a counter electrode and a mercury/mercuric oxide electrode as the reference electrode. All experiments were conducted in ambient conditions. Prior to the coating, the RDE were polished with 1 μm and 0.05 μm alumina powder (MicroPolish, Buehler) slurry with subsequent ultrapure water washing followed by removal of the alumina through sonication of the RDE in isopropanol and DI water for 2 minutes, respectively. The polished RDE was dried under N_2-stream and the ink slurry was drop cast from a catalyst suspension. The suspension consisted of 4 mg of metal oxide, 1587 mg of DI water (1590 μL), 312 mg of isopropanol (400 μL) and 8.6 mg of Nafion D-520 dispersion (9.04 μL, 5 wt%, Sigma-Aldrich). After homogenization, 9.82 μL of the suspension was dropped onto the RDE and was dried in air.

Results and discussion

The doping level of the secondary metals for this study is represented by the nomenclature "1% M NiO", where M = Co, Fe, Mn and the value represent the mole percent to the whole. In this study, the inclusion of the secondary metals will be referred to as doping rather than mixing. The metal ratios were determined through ICP-OES and samples measured were within 2% of the theoretical value for all samples tested (Table S1†). The size of the nanosheets and both the area and quantity of the holes are controlled through the preparation conditions. Specifically, the size of the nanosheets is affected by the urea concentration, with higher concentrations of urea yielding smaller nanosheets. Benzyl alcohol has several functions in the synthesis. It acts as a structure directing agent, promoting the growth of the (111) facet. It is also necessary to form hexagonal holes with none forming in its absence. The annealing temperature of $Ni(OH)_2$ plays a critical role in determining both the morphology and porosity of the resulting nanosheets. Higher annealing temperatures lead to a reduction in overall sheet size while simultaneously increasing both the diameter and abundance of the hexagonal holes. These conditions have been detailed in previous studies.[11,16]

The supercritical process is important to preserve the surface area of the nanosheets while promoting the mixing of the metals in a high mobility environment. Due to the properties of the solvent at the supercritical state, the reaction occurs in an environment with much higher mass diffusion allowing for faster diffusion of the reactants than found in a traditional liquid environment.[33,34] At the release of the supercritical gas, the rapid mass transfer of methanol from within the powder moves towards the surface and inert gas (in this case Ar) flows in to replace it. This pseudo-supercritical drying better maintains the synthesized microstructure as there is minimal interaction of the solvent

with the products during the drying step due to the density of the gas having liquid-like behaviour but exerting no capillary forces.[11] The majority of latent reactants still in the solvent will also be removed from the system, removing the need for the washing of the as-prepared product.

The crystallinity and phase purity of the catalysts were analysed using PXRD (Fig. 1). The as-synthesized product is crystalline with a strong peak around 12 2θ which is characteristic for α-$Ni(OH)_2$ (Fig. S1†). The full phase transformation from α-$Ni(OH)_2$ to NiO occurs at annealing temperatures above 273 °C.[11] The reflexes at 37, 43, 64, 75, and 79 2θ corresponds to the (111), (002), (220), (311), and (222) crystal planes and is characteristic of the $Fm\bar{3}m$ rock salt space group.[35] The introduction of dopants slightly effects the lattice parameters of the rock salt. The inclusion of Co slightly lowers the peak positions of the (111) reflex indicating an expansion of the lattice. The introduction of Mn and Fe results in a similar but less pronounced change in the peak position meaning a smaller expansion of the lattice (Table S2†). The lattice expansion of NiO from dopant incorporation has been reported in previous studies.[36–38] This is attributed to the larger cationic radii of the dopants: Fe^{2+} (0.77 Å), Mn^{2+} (0.80 Å), and Co^{2+} (0.72 Å) are all larger than that of Ni^{2+} (0.69 Å).[39] It should be noted for all dopants that the presence of a higher oxidation state would result in lattice contraction, not expansion. For instance, Fe^{3+} has a cationic radius of 0.63 Å, and the observed lattice expansion suggests that iron is predominantly incorporated in the +2 oxidation state. When assessing crystalline homogeneity, Co has no impurity peaks which can be attributed to the stability of Co^{2+} and its structural compatibility with NiO, as CoO also adopts a rock salt crystal structure. However, the 10% Mn and 10% Fe samples contain alternate peaks which correspond to Fe_2O_3 and Mn_2O_3 respectively. Fe_2O_3 is observed likely due to the use of an Fe^{3+} precursor which undergoes hydrolysis at a much faster rate than Ni^{2+}, which is discussed below.[40] Mn also readily oxidizes to a 3^+ state, resulting in the formation of Mn_2O_3 as well as the doped NiO.[41]

The (111) facet of NiO is confirmed through high-resolution transmission electron microscopy (HRTEM). The calculated *d*-spacing for the (111) facet of NiO has been previously reported as 2.41 Å (Fig. 2g).[42] All samples measured *d*-spacings are consistent with this value within error (Fig. 2h). As the concentration of dopant increases, the *d*-spacing expands slightly with the largest deviation over the pristine material of 3.8% seen in 10% Mn NiO(111). All dopants result in an increase in the *d*-spacing of the material relative to undoped NiO. This is consistent with the finding from PXRD that lattices are expanding with the inclusion of dopants. Furthermore, changes to crystallinity occur as the concentration of dopants increase. Increasing dopant concentrations lead to a progressive loss of crystallinity relative to pristine NiO(111). This loss of crystallinity is theorized to be from the increase in number of defects within the material caused by dopant introduction as well as

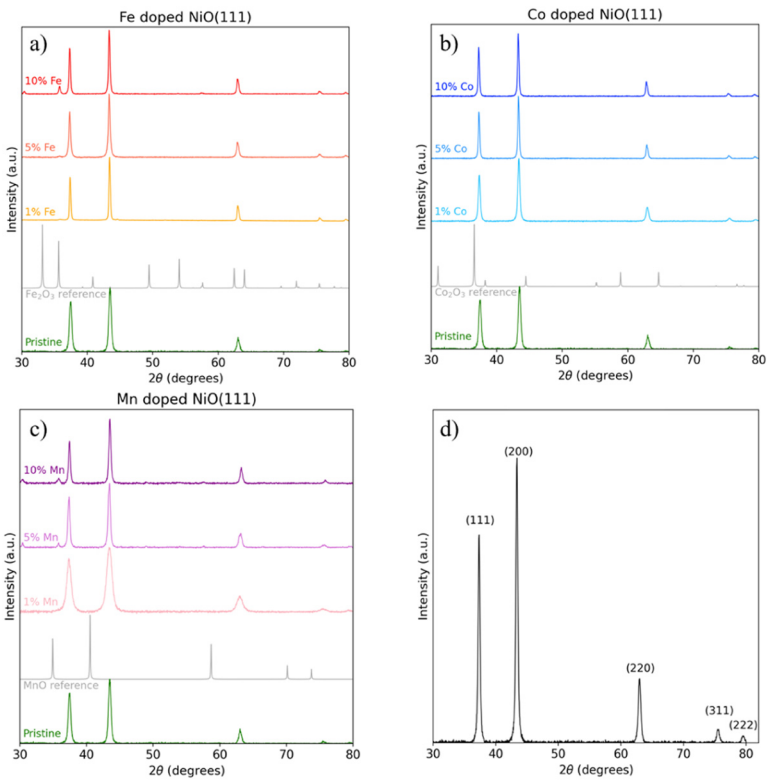

Fig. 1 Powder X-ray diffraction (PXRD) patterns of a) Co, b) Fe, c) Mn doped NiO(111) catalysts. Secondary peaks are seen in the Mn and Fe samples corresponding to separate oxides. d) Index of the planes for the NiO diffraction pattern.

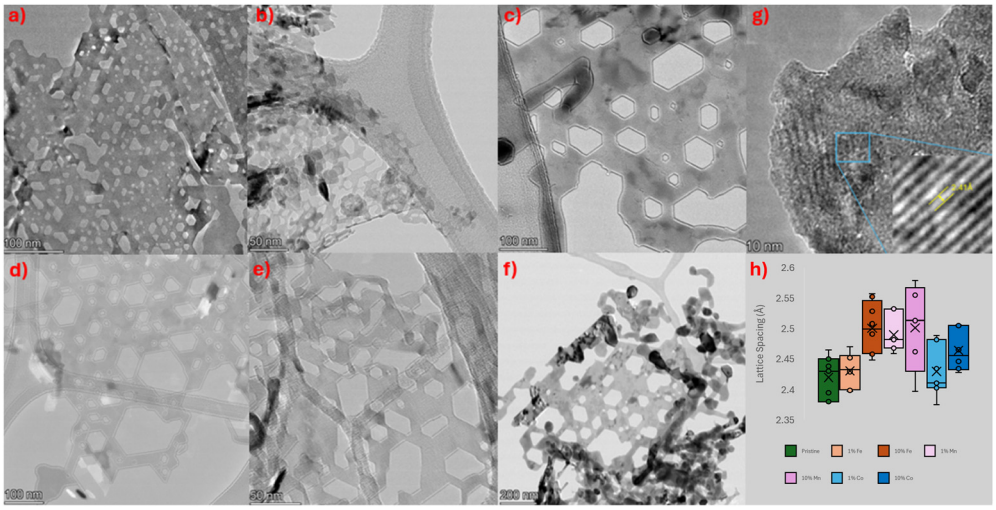

Fig. 2 Transmission electron microscopy (TEM) images of 5% a) Mn, b) Fe, and c) Co and 10% d) Mn, e) Fe, and f) Co NiO. g) High resolution TEM image with an example lattice fringe measurement on pristine NiO(111). h) Candlestick plot with the average *d*-spacing for the various Ni samples taken over minimum 8 locations.

differences in cationic radii introducing localized areas of strain which disrupt the long-range order.[37,43]

Upon inclusion of dopants, the NiO(111) sheets appear to thicken. This phenomena has been reported previously.[23,44] A change in crystallite sizes is also observed, with crystals increasing in size with the inclusion of a secondary metal and with higher loadings resulting in greater increases (Table S3†). SEM images reveal that doping appears to increase the 2D surface area resulting in larger nanosheets (Fig. S2†). Interestingly, changes in crystallite size do not result in a significant change in surface area. Mn induces the greatest change, with higher doping levels resulting in an increase in surface area. Beyond dopant-influenced vacancies, the differences in cation size introduce localized strain within the crystal lattice, disrupting long-range order.[45] The N_2 linear isotherms exhibit nonporous character which is consistent with the presence of holes not porosity (Fig. S3†). All TEM images show nanosheets with hexagonally shaped holes present. The hole size within the nanosheets varies depending on the specific dopant introduced. The as-prepared α-$Ni(OH)_2$ does not have any voids prior to calcination (Fig. S4†). When cobalt is incorporated, the holes are significantly larger (50–200 nm diameter) compared to the other doped systems and closely resemble those observed in pristine NiO. In contrast, Mn and Fe-doped samples form much smaller holes, with the average diameter closer to 50 nm.

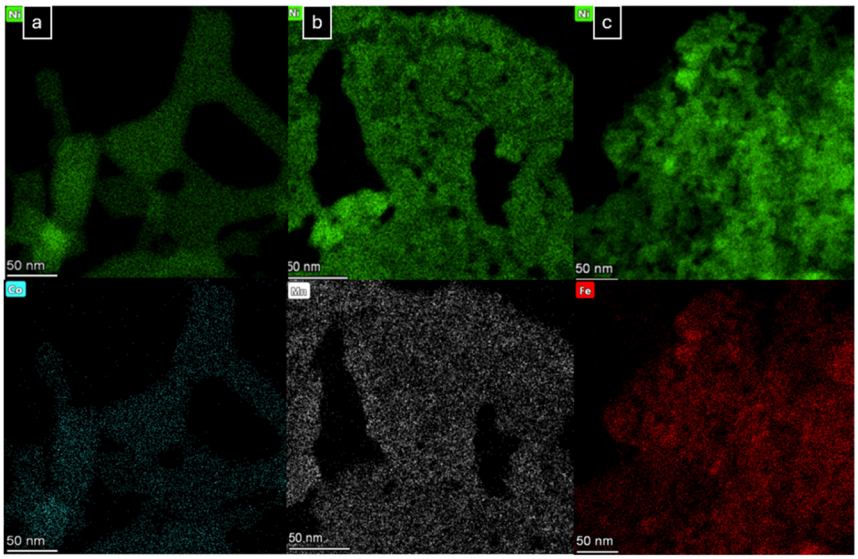

Fig. 3 STEM-EDS maps of a) 10% Co, b) 10% Mn, and c) 10% Fe NiO(111) showing the distribution of the dopants across the NiO sheets.

Elemental mapping confirms the dispersion of dopants is uniform for all metals (Fig. 3). These were uniformly incorporated into single phase NiO(111) at low doping levels with an unaltered synthesis protocol. However, secondary phases appeared at doping levels above 5% for Fe and Mn. The solution pH was found to be a critical factor on the final homogeneity of the material. This is due to the dual influence of pH on hydrolysis and condensation. An acidic system catalyses hydrolysis while subsequently repressing condensation, and the opposite is true in an alkaline enviroment.[46] This results in denser gels in acidic conditions and lighter gels in an alkaline processes. Typically, the parent synthesis was performed in an acidic environment because the precursor salts, nitrates, would react with the water and form nitric acid while hydrolysis is occurring.[16] This is observed at the inclusion of the salts with a drop in pH occurring soon after addition to the aqueous solution resulting in a promotion of the hydrolysis of Ni^{2+}. However, this enhanced hydrolysis facilitates the independent formation of nickel and iron oxide phases, rather than enabling the uniform incorporation of Fe into the NiO lattice. Shah *et al.* reported the formation of mixed Fe_2O_3 and Fe_3O_4 forming at low pH while forming single phase Fe_3O_4 in an alkaline environment.[47] The formation of multiple phases is hypothesized to be due to the differences in the rates of hydrolysis of the various metal precursors. Among the different metal cations, the hydrolysis rates vary: Fe^{3+}: −12 kcal mol^{-1}, Ni^{2+}: −19.2 kcal mol^{-1}, Co^{2+}: −19.7 kcal mol^{-1}, Mn^{2+}: −22.2 kcal mol^{-1}.[40] Of the dopants, Fe^{3+} shows the greatest deviation in rate, which is likely a key factor behind the formation of a secondary Fe_2O_3 phase. The higher oxidation state of the Fe results in a more rapid formation of the M–OH bond over Ni^{2+} favouring phase segregation. However, when the pH of the synthesis was adjusted to approximately 5, the formation of the undesired iron oxide phase was suppressed and a larger share of the desire NiO phase was formed. An Fe^{3+} precursor is used because free NO_3^- is more readily evacuated by supercritical drying than Cl^-.[18]

The samples were examined by X-ray absorption spectroscopy (XAS) experiments before and after (aEC) electrochemistry treatment to determine the differences in the oxidation state of the metal centres as the surface became electrochemically active. It is known that the surface reconstructs to an oxyhydroxide form when subjected to electrochemical conditions which implies an oxidation of the Ni metal during the catalytic process.[22] The X-ray absorption near edge structure (XANES) showed no new features with doping but the positions of the edge (at 0.5 intensity) shifted with doping (Fig. 4a) and electrochemical treatment (Fig. 4b) relative to that of pristine NiO(111). The position of the maximum (so called white line) moved to lower energy with electrochemical treatment (Fig. 4b), except for Co-doping, which might indicate a change in protonation due to electrochemical treatment where it is shifted. The variations of the edge position were further studied by the integral

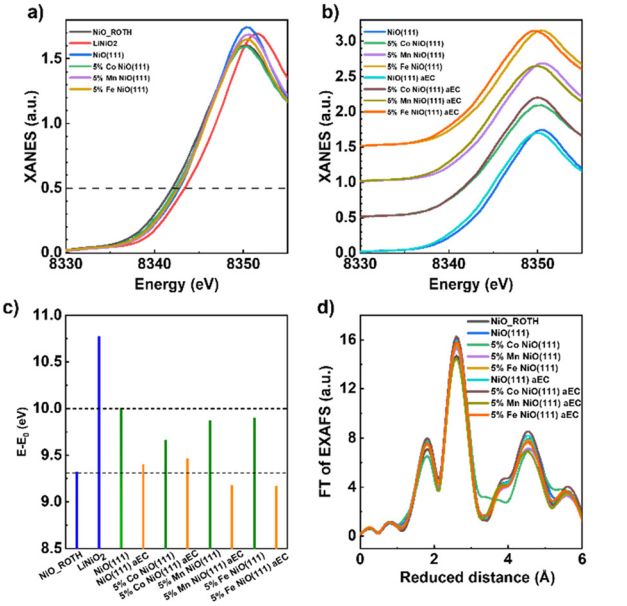

Fig. 4 (a) X-ray absorption near edge structure (XANES) spectra at Ni-K edge for pristine NiO(111), Co, Fe and Mn-doped NiO(111) and commercial references NiO_ROTH and $LiNiO_2$. (b) XANES of doped NiO(111) before and after electrochemical treatment (aEC). The spectra were offset for clarity. (c) Integral edge positions relative to E_0 = 8333 eV for doped and aEC samples. Olive green, orange and blue represent pristine, aEC samples and references, respectively. (d) Fourier transform (FT) of extended X-ray absorption fine structure (EXAFS) spectra at the Ni-K edge for doped and aEC samples and commercial NiO_ROTH.

method to discuss trends in oxidation.[48] The edge position relative to Ni metal (E–E_0) of NiO(111) is between that of the commercial NiO and $LiNiO_2$ samples suggesting an oxidation state between 2^+ and 3^+. Doping reduced the edge position slightly with the strongest effect seen for Co doping. The inclusion of these secondary metals results in thicker nanosheets but also likely increased amounts of defects, specifically oxygen vacancies, which may explain the observed differences in edge position and slight Ni reduction. Electrochemical treatment resulted consistently in lower edge positions shown in Fig. 4c and thus further Ni reduction. The lowest edge positions were found for Mn and Fe doping where they were slightly below the NiO reference, although having a lower white line position and thus spectra change as aforementioned. Thus, we refrain from giving explicit values of the Ni oxidation state because we cannot rigorously assign the edge shift uniquely to it. Additionally, the extended X-ray absorption fine structure (EXAFS) (Fig. 4d) was analysed where the position and amplitude of the peaks in the Fourier transformed spectra did not vary with doping or electrochemical treatment and conform to that of the commercial NiO reference in agreement with PXRD analysis. The analysis of the NiO(111)-aEC sample is important as it will show how the material chemically changes during the oxidation and reduction of the catalysts surface. For all samples, after cycling on a rotating disk electrode (RDE) the

peaks shift towards a reduction in the metal. The reduction was so much in fact that the peaks end up at lower energies than the Ni^{2+} reference material. During electrolysis, the active surface for the OER for NiO is Ni(OOH). Meaning the surface species of the catalyst oxidized under working conditions. Note that XAS and PXRD are bulk methods that are unlikely to resolve surface oxidation.

Electrochemistry

For the OER, studies have been conducted on thin film spin coated NiO sheets. When performing cyclic voltammetry in a basic media (1 M KOH), an oxidation peak around 0.38 V and reduction peaks occur around −0.34 V and −0.10 V correspond to the Ni^{2+}/Ni^{3+} charge transition (Fig. 5). During the forward scan, OH^- was observed to be intercalating into the NiO film and removed during the reverse scan. RDE experiments were conducted using glassy carbon substrate (GC) electrodes with a 4 mm diameter. Linear sweep voltammetry was used as a screening method of OER catalytic activity for the doped samples. Here, the most immediate activity observation is the difference in the positive impact of 5% Co- and Fe-doped samples *versus* the deleterious effects of Mn-doping on the activity displayed. When comparing with the pristine NiO_x nanosheets, 5% Fe–NiO_x shows the largest improvement in activity both before and after activation cycling followed by 5% Co–NiO_x with less improvement. In sharp contrast to the Fe and Co-doped samples however, 5% Mn–NiO_x shows a sharp decrease in activity compared to the pristine NiO_x nanosheets before cycling that only further worsens after the activation cycling step.

Using the common electrode activity benchmark of comparing potential at 10 mA cm^{-2},[49] the improved activity of the 5% Fe and Co-doped samples can be seen in their overpotentials of 457 mV and 502 mV after cycling respectively. These are both substantial improvements over the pristine NiO_x overpotential of 541 mV after cycling. Similar activities are reported for comparable catalysts at the same benchmark (Table S4†). In addition to 10 mA cm^{-2}, the catalyst overpotentials are reported at 2 mA cm^{-2} and the current densities are recorded at 1.55 V (Tables S5 and S6†). Pebley *et al.* observed a reduction in overpotential of around 15% with inclusion of any amount of Fe into deposited NiO nanocatalysts but saw inconsistent activity trend with varying concentrations of Fe.[50] The understanding of these trends is difficult because even the identification of the exact active site in Ni–Fe systems is debated in literature. Chung *et al.* found that MOH–Fe interaction is key to activity with Fe becoming the more active species in the system due to a lower activation energy needed to oxidize and accommodate the M–(OOH) active surface.[51] Alternatively, Li *et al.* put forward that the Ni is the active site with Fe promoting the formation of higher valent surface Ni, and Görlin *et al.* posits that the Fe stabilizes the low-valence Ni sites, resulting in a suppression of the Ni oxidation to lower values.[52,53] When exploring the other positive trend, improvements from Co have been seen in other systems as well. Vazhayil *et al.* reported improvements of up to 300 mV over pristine NiO when incorporating Co due to improvements to both the mass activities of the material as well as reduction in the reaction resistance of the catalyst which has been seen in other studies as well.[54,55] Alternatively, Bhanja *et al.* found that the inclusion of Co increases activity as the NiOOH has worse reaction kinetics than CoOOH resulting in better activity with exposed Co active sites on the surface.[56]

On the opposite trend, 5% Mn–NiO_x further shows its negative effects on OER activity by not reaching 10 mA cm^{-2} before the end of the cycling window, where the highest current density it reaches is 6.7 mA cm^{-2} at 1.945 V. Also, Mn resulted in a decrease in electrode activity after activation cycling with the maximum current density recorded 4.713 mA cm^{-2} at 1.962 V. A reduction in activity due to Mn incorporation into NiO has been previously seen in literature.[51] A series of Ni and Co layered double hydroxides were previously studied for the OER by Dionigi and Mn performed the worst of the tested metals for Ni-LDHs. This was found to be due to the reaction free energy at 1.23 eV for

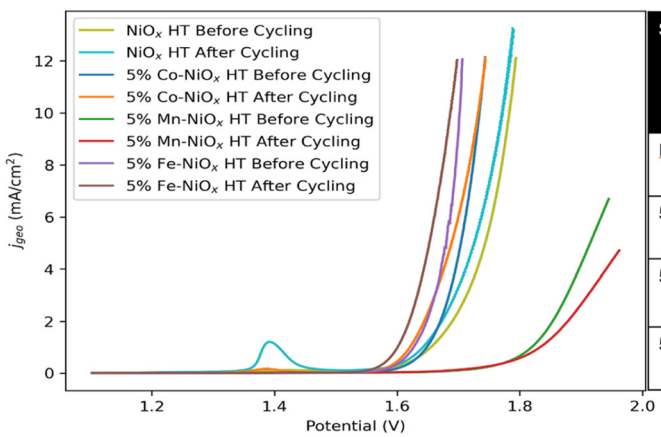

Sample	Overpotential @ 10mA/cm² before cycling (mV)	Overpotential @ 10mA/cm² after cycling (mV)
NiO	553	541
5% Co NiO	504	502
5% Mn NiO	715	742
5% Fe NiO	472	457

Fig. 5 Rotating disc electrode experiments of various NiO before and after electrochemical cycling. The overpotentials at 10 mA cm^{-2} are listed to the right.

the two-metal coordination of OH*. DFT calculations had shown that these two-metal sites would be more favourable than a single-metal coordination environment but resulted in worse reaction kinetics when experimentally tested with Mn–Ni.[57] The conclusion was that Ni–Ni sites had higher activity than Mn–Ni and doping Mn on the surface reduced the density of these sites. The reduction in activity after cycling the Mn sample is predicted to be due to oxidative leaching of the Mn from the surface during cycling. Leaching of Mn from the surface of NiO has previously been shown *via* the oxidation of the Mn on the surface into MnO_4^- which the dissolves into solution which results in the loss of metal sites on the surface.[58]

In comparison to other high performing catalysts, crystalline RuO has previously reported to have an overpotential of 480 mV while Ir/C reported as 440 mV at 10 mA cm^{-2} showing the 5% Fe sample is competitive with the current benchmarks at the same current density.[59] However, previous NiFeO nanoparticles have reported overpotentials as low as 300 mV.[60] Finally, while pristine NiO_x after cycling is outperformed by both 5% Fe and Co, it is interesting to note that it shows the largest oxidation peak at 1.4 V which is a peak commonly attributed to the $Ni^{2+\rightarrow 3+}$ oxidation.[61] The lack of this large oxidation peak in the 5% Fe and Co-doped samples indicates that these additional transition metal samples are suppressing this Ni oxidation step while still positively contributing to the overall catalytic activity.

Conclusion

This study set out to explore the synthesis and characterization of doped NiO(111) nanosheets as promising OER catalysts in AEM electrolyzers by leveraging their high surface oxygen density, interesting surface morphology, and active dopant species dispersed by a unique supercritical method. The alkaline enviroment of an AEM system enables the use of a broader variety of alternative catalysts that can compete with the top-performing PGM metals (Ir, Ru) in PEM systems. Given the potential of viable cost-effective AEM catalysts, understanding their capabilities by varying morphologies, chemical surfaces, and metal compositions are essential to advancing the fundumental understanding of these systems. The pre-catalyst NiO(111) nanosheets were prepared *via* a highly mobile and protective supercritical sol–gel process. The inclusion of dopants did not result in large-scale change of the morphology of the pristine material but characteristic physical traits were slightly altered with their introduction. As the dopant level increased, the crystallinity of the NiO decreased as determined by XRD, and the presence of a small amount of secondary phases appeared within the bulk for Fe and Mn. The crystallite size was also affected with the crystallite size increasing but surface area having no clear trend. TEM was performed to visualize the changes of the dopants to the morphology with all nanosheets increasing in thickness with their addition. Despite small impurities, the predominant phase observed was the (111) nanosheet as confirmed by HRTEM. The expansion of the lattice was also corroborated by HRTEM and showed a relatively novel technique in semi-quantitiatively calculating lattice alteration. EDS mapping showed good dispersion of the elements throughout the system. XAS revealed that the NiO slightly oxidized with the inclusion of the dopants. However, after cycling in an RDE setup there was a noticable reduction in the sample to below even the pristine NiO. Initial electrochemical screening revealed that Fe incorporation resulted in the largest reduction to the overpotential of the pristine catalyst and Co inclusion producing less significant improvements. The Mn-doped samples, on the other hand, greatly diminished the activity of the catalyst and drastically increased the overpotential. Overall, it was observed that the inclusion of transition metal dopants has the potential to increase the electrochemical activity of NiO(111) nanosheets with hexagonal holes depending on the cation. This work contributes to the broader understanding of nanoscale AEM catalysts by investigating how the introduction of dopants affects a novel NiO(111) nanosheets for the OER. NiO is a potential cost-effective competative catalyst that can support a viable large-scale deployment of electrolysis if succifient activities can be reached. Both Co- and Mn-doped NiO systems and unsupported NiO nanosheets are underexplored in this research area and cataloging of the morphological evolution will aid in the design for next-generation water-splitting technologies.

Data availability

All data available upon request to corresponding author.

Author contributions

Brim, E., wrote original draft, investigation, data curation, software, formal analysis, and validation. Hayes, D. W., Ruecker, K., Taffa, D. H., and Bisen, O.: support in synthesis, data curation, software, formal analysis and validation. Alia, S., Risch, M., Lorenz, J., Harms, C., Wark, M.: supervision, project administration, and resources. Richards, R.: conceptualization, project administration, and supervision. Paper was reviewed and edited by all participants.

Conflicts of interest

The authors declare no financial or personal conflicts of interest in the work reported in this paper.

Acknowledgements

This work was funded and financially supported by the collaboration of the National Science Foundation (NSF) and the German Research Foundation (DFG, Deutsche Forschungsgemeinschaft) on grant CBET-2139971 and grant 460244535, respectively. Additional support came from the NSF INTERN supplement received by Elliot Brim. The authors

acknowledge and are thankful for the support of the Colorado School of Mines, National Renewable Energy Laboratory (NREL), University of Oldenburg, the German Aerospace Center (DLR), and the Helmholtz Zentrum Berlin (HZB). Furthermore, We thank the Helmholtz-Zentrum Berlin für Materialien und Energie for the allocation of synchrotron radiation beamtime and G. Schuck for support at the beamline KMC-2. Further, we acknowledge Imke Mönkeberg (DLR), Jasmin Schmeling (University of Oldenburg), N. N. (HZB) for the support during the beam time. This work was in part authored by the National Renewable Energy Laboratory, operated by Alliance for Sustainable Energy, LLC, for the U.S. Department of Energy (DOE) under Contract No. DE-AC36-08GO28308. The views expressed in the article do not necessarily represent the views of the DOE or the U.S. Government. The U.S. Government retains and the publisher, by accepting the article for publication, acknowledges that the U.S. Government retains a nonexclusive, paid-up, irrevocable, worldwide license to publish or reproduce the published form of this work, or allow others to do so, for U.S. Government purposes.

References

1 D. Deng, K. S. Novoselov, Q. Fu, N. Zheng, Z. Tian and X. Bao, *Nat. Nanotechnol.*, 2016, **11**, 218–230.
2 T. Li, T. Jing, D. Rao, S. Mourdikoudis, Y. Zuo and M. Wang, *Inorg. Chem. Front.*, 2022, **9**, 6008–6046.
3 A. M. Oliveira, R. R. Beswick and Y. Yan, *Curr. Opin. Chem. Eng.*, 2021, **33**, 100701.
4 S. B. Somwanshi, S. B. Somvanshi and P. B. Kharat, *J. Phys.: Conf. Ser.*, 2020, **1644**, 012046.
5 S. Jung, C. C. L. McCrory, I. M. Ferrer, J. C. Peters and T. F. Jaramillo, *J. Mater. Chem. A*, 2016, **4**, 3068–3076.
6 D. Xu, M. B. Stevens, M. R. Cosby, S. Z. Oener, A. M. Smith, L. J. Enman, K. E. Ayers, C. B. Capuano, J. N. Renner, N. Danilovic, Y. Li, H. Wang, Q. Zhang and S. W. Boettcher, *ACS Catal.*, 2019, **9**, 7–15.
7 L. Osmieri, J. Park, D. A. Cullen, P. Zelenay, D. J. Myers and K. C. Neyerlin, *Curr. Opin. Electrochem.*, 2021, **25**, 100627.
8 J. Chen, L. Shi, L. Du, S. Ye and S. Zhao, *Chem Catal.*, 2023, **3**, 100733.
9 G. F. McLean, T. Niet, S. Prince-Richard and N. Djilali, *Int. J. Hydrogen Energy*, 2002, **27**, 507–526.
10 L. Yang, J. Heinlein, C. Hua, R. Gao, S. Hu, L. Pfefferle and Y. He, *Fuel*, 2022, **324**, 124706.
11 D. H. Taffa, E. Brim, K. K. Rücker, D. Hayes, J. Lorenz, O. Bisen, M. Risch, C. Harms, R. M. Richards and M. Wark, *ACS Appl. Mater. Interfaces*, 2024, **16**, 62142–62154.
12 R. A. Krivina, Y. Ou, Q. Xu, L. P. Twight, T. N. Stovall and S. W. Boettcher, *Acc. Mater. Res.*, 2021, **2**, 548–558.
13 C. Wang, P. Zhai, M. Xia, W. Liu, J. Gao, L. Sun and J. Hou, *Adv. Mater.*, 2023, **35**, e2209307.
14 A. Govind Rajan, J. M. P. Martirez and E. A. Carter, *J. Am. Chem. Soc.*, 2020, **142**, 3600–3612.
15 S.-J. Hong, H.-J. Mun, B.-J. Kim and Y.-S. Kim, *Micromachines*, 2021, **12**, 1168.
16 J. Hu, K. Zhu, L. Chen, H. Yang, Z. Li, A. Suchopar and R. Richards, *Adv. Mater.*, 2008, **20**, 267–271.
17 J. Hu, K. Zhu, L. Chen, C. Kübel and R. Richards, *J. Phys. Chem. C*, 2007, **111**, 12038–12044.
18 Z. Song, L. Chen, J. Hu and R. Richards, *Nanotechnology*, 2009, **20**, 275707.
19 M. D. Susman, H. N. Pham, X. Zhao, D. H. West, S. Chinta, P. Bollini, A. K. Datye and J. D. Rimer, *Angew. Chem., Int. Ed.*, 2020, **59**, 15119–15123.
20 F. Lin, D. Nordlund, T.-C. Weng, R. G. Moore, D. T. Gillaspie, A. C. Dillon, R. M. Richards and C. Engtrakul, *ACS Appl. Mater. Interfaces*, 2013, **5**, 301–309.
21 Z. Xiao, W. Zhou, B. Yang, C. Liao, Q. Kang, G. Chen, M. Liu, X. Liu, R. Ma and N. Zhang, *Nano Mater. Sci.*, 2023, **5**, 228–236.
22 M. Görlin, P. Chernev, J. Ferreira de Araújo, T. Reier, S. Dresp, B. Paul, R. Krähnert, H. Dau and P. Strasser, *J. Am. Chem. Soc.*, 2016, **138**, 5603–5614.
23 A. Etxebarria, M. Lopez Luna, A. Martini, U. Hejral, M. Rüscher, C. Zhan, A. Herzog, A. Jamshaid, D. Kordus, A. Bergmann, H. Kuhlenbeck and B. Roldan Cuenya, *ACS Catal.*, 2024, **14**, 14219–14232.
24 L. Trotochaud, S. L. Young, J. K. Ranney and S. W. Boettcher, *J. Am. Chem. Soc.*, 2014, **136**, 6744–6753.
25 B. Paul, P. Bhanja, S. Sharma, Y. Yamauchi, Z. A. Alothman, Z.-L. Wang, R. Bal and A. Bhaumik, *J. Colloid Interface Sci.*, 2021, **582**, 322–332.
26 Y. Wang, A. Kumar, E. Budiyanto, H. Cheraparambil, C. Weidenthaler and H. Tüysüz, *ACS Appl. Energy Mater.*, 2024, **7**, 3145–3156.
27 T. Priamushko, P. Guggenberger, A. Mautner, J. Lee, R. Ryoo and F. Kleitz, *ACS Appl. Energy Mater.*, 2022, **5**, 13385–13397.
28 I. M. Abdulagatov, N. G. Polikhronidi, A. Abdurashidova, S. B. Kiselev and J. F. Ely, *Int. J. Thermophys.*, 2005, **26**, 1327–1368.
29 İ. Şahin, Y. Özbakır, Z. İnönü, Z. Ulker and C. Erkey, *Gels*, 2017, **4**, 3.
30 G. A. Mutch, S. Shulda, A. J. McCue, M. J. Menart, C. V. Ciobanu, C. Ngo, J. A. Anderson, R. M. Richards and D. Vega-Maza, *J. Am. Chem. Soc.*, 2018, **140**, 4736–4742.
31 D. M. Többens and S. Zander, *Journal of large-scale research facilities JLSRF*, 2016, **2**, A49.
32 O. Y. Bisen, M. Baumung, M. Tatzel, C. A. Volkert and M. Risch, *Energy Adv.*, 2024, **3**, 504–514.
33 P. E. Savage, S. Gopalan, T. I. Mizan, C. J. Martino and E. E. Brock, *AIChE J.*, 1995, **41**, 1723–1778.
34 S. N. Gonzalez, C. McFadden Block, R. P. O'Hayre and R. M. Richards, *Langmuir*, 2024, **40**, 23573–23582.
35 F. Fazlali, A. reza Mahjoub and R. Abazari, *Solid State Sci.*, 2015, **48**, 263–269.
36 K. Fominykh, P. Chernev, I. Zaharieva, J. Sicklinger, G. Stefanic, M. Döblinger, A. Müller, A. Pokharel, S. Böcklein, C. Scheu, T. Bein and D. Fattakhova-Rohlfing, *ACS Nano*, 2015, **9**, 5180–5188.

37 W. Moschkowitsch, N. Zion, H. C. Honig, N. Levy, D. A. Cullen and L. Elbaz, *ACS Catal.*, 2022, **12**, 12162–12169.
38 K. Cysewska, M. Zając, M. Łapiński, J. Karczewski, M. K. Rybarczyk, B. Kamecki, P. Jasiński and S. Molin, *Energy Technol.*, 2021, **9**, 2100688.
39 R. D. Shannon, *Acta Crystallogr., Sect. A*, 1976, **32**, 751–767.
40 P. Brown and C. Ekberg, *Hydrolysis of Metal Ions*, 2016, vol. 1.
41 T. L. Rakitskaya, A. Truba, G. Dzhyga, A. Nagaevs'ka and V. Volkova, *Colloids Interfaces*, 2018, **2**, 61.
42 A. R. Balu, V. S. Nagarethinam, N. Arunkumar and M. Suganya, *J. Electron Devices*, 2012, **13**, 920–930.
43 M. Nozari-Asbemarz, M. Amiri, H. Imanzadeh, A. Bezaatpour, S. Nouhi, P. Hosseini, M. Wark and D. Seifzadeh, *Int. J. Hydrogen Energy*, 2022, **47**, 5250–5259.
44 Y. H. Teferi, B. A. Gonfa, F. K. Sabir and L. T. Tufa, *Chem. Phys. Impact*, 2025, **10**, 100831.
45 R. Islam, R. Abdur, M. A. Alam, N. Munna, A. N. Ahmed, M. Hossain, M. S. Bashar, D. Islam and M. S. Jamal, *Nanoscale Adv.*, 2024, **7**, 133–143.
46 T. Esquivel-Castro, A. Martinez-Luevanos, S. Estrada and L. Cano-Salazar, *Porous Materials for Applications in Energy and Enviroment*, 2020.
47 S. Z. H. Shah, U. Khan, S. Riaz and S. Naseem, *Mater. Today: Proc.*, 2015, **2**, 5214–5219.
48 H. Dau, P. Liebisch and M. Haumann, *Anal. Bioanal. Chem.*, 2003, **376**, 562–583.
49 C. C. L. McCrory, S. Jung, J. C. Peters and T. F. Jaramillo, *J. Am. Chem. Soc.*, 2013, **135**, 16977–16987.
50 A. C. Pebley, E. Decolvenaere, T. M. Pollock and M. J. Gordon, *Nanoscale*, 2017, **9**, 15070–15082.
51 D. Y. Chung, P. P. Lopes, P. Farinazzo Bergamo Dias Martins, H. He, T. Kawaguchi, P. Zapol, H. You, D. Tripkovic, D. Strmcnik, Y. Zhu, S. Seifert, S. Lee, V. R. Stamenkovic and N. M. Markovic, *Nat. Energy*, 2020, **5**, 222–230.
52 N. Li, D. K. Bediako, R. G. Hadt, D. Hayes, T. J. Kempa, F. von Cube, D. C. Bell, L. X. Chen and D. G. Nocera, *Proc. Natl. Acad. Sci. U. S. A.*, 2017, **114**, 1486–1491.
53 M. Görlin, P. Chernev, J. Ferreira de Araújo, T. Reier, S. Dresp, B. Paul, R. Krähnert, H. Dau and P. Strasser, *J. Am. Chem. Soc.*, 2016, **138**, 5603–5614.
54 A. Vazhayil, S. Ashok C, J. Thomas and N. Thomas, *Mater. Chem. Phys.*, 2023, **300**, 127540.
55 J. Zhang, G. Cai, D. Zhou, H. Tang, X. Wang, C. Gu and J. Tu, *J. Mater. Chem. C*, 2014, **2**, 7013–7021.
56 P. Bhanja, B. Mohanty, B. Paul, A. Bhaumik, B. K. Jena and S. Basu, *Electrochim. Acta*, 2022, **416**, 140277.
57 F. Dionigi, J. Zhu, Z. Zeng, T. Merzdorf, H. Sarodnik, M. Gliech, L. Pan, W.-X. Li, J. Greeley and P. Strasser, *Angew. Chem., Int. Ed.*, 2021, **60**, 14446–14457.
58 K. K. Rücker, D. H. Taffa, O. Bisen, M. Risch, D. Hayes, E. Brim, R. M. Richards, C. Harms, M. Wark and J. Lorenz, *J. Phys. Chem. C*, 2025, **129**, 9341–9355.
59 Y. Duan, Z.-Y. Yu, S.-J. Hu, X.-S. Zheng, C.-T. Zhang, H.-H. Ding, B.-C. Hu, Q.-Q. Fu, Z.-L. Yu, X. Zheng, J.-F. Zhu, M.-R. Gao and S.-H. Yu, *Angew. Chem., Int. Ed.*, 2019, **58**, 15772–15777.
60 G. Shi, C. Arata, D. A. Tryk, T. Tano, M. Yamaguchi, A. Iiyama, M. Uchida, K. Iida, S. Watanabe and K. Kakinuma, *ACS Omega*, 2023, **8**, 13068–13077.
61 D. Hayes, S. Alia, B. Pivovar and R. Richards, *Chem Catal.*, 2024, **4**, 100905.